Aeroacoustics Conferences
20-23 May 2019, Delft, The Netherlands
25th AIAA/CEAS Aeroacoustics Conference
10.2514/6.2019-2604

New modular fan rig for advanced aeroacoustic tests - Modal decomposition on a 20'' UHBR fan stage

A. Pereira* and E. Salze†
Univ Lyon, Ecole Centrale de Lyon, LMFA & UMR CNRS 5509, 69134 Ecully, France.

J. Regnard‡, F. Gea-Aguilera§ and M. Gruber¶
Safran Aircraft Engines, Département Aérodynamique et Acoustique, 77550 Moissy Cramayel, France.

This paper presents a methodology to estimate the fan modal content based on in-duct acoustic measurements. These measurements were performed on a 20" UHBR fan rig designed and manufactured together by Safran Aircraft Engines and Ecole Centrale de Lyon. The dedicated instrumentation includes a number of rotating microphone arrays, which allows for fine-tuned spatial discretizations while using a relatively reduced number of microphones. The difficulty of sequential measurements is that phase relationships between moving microphones at successive acquisitions are not measured. A technique for the reconstruction of phase relationships is evaluated using experimental data. The modal content has been evaluated at various fan stage locations, including the intake, fan/OGV inter-stage and downstream of the OGVs.

I. Introduction

To reduce the fuel burn consumption of aircraft engines, future architectures tend to increase the bypass ratio. The next generation of turbojet engines, present an Ultra High Bypas Ratio (UHBR). This results in a widening of the fan diameter which is associated with a reduction of the fan rotation speed, the exhaust jet speed and the nacelle length. The consequences on fan noise are threefold. Firstly, the reduction of exhaust jet speed modifies the relative contribution of the noise sources, such that fan noise is expected to be the main noise source. Secondly, fan noise generation could be more challenging to predict with a short inlet due to the influence of the inflow distortion. Finally, the reduction of rotation speed implies a shift of acoustic energy towards lower frequencies, which are difficult to attenuate with conventional acoustic liners in a short nacelle. Therefore, UHBR turbofan engines present several acoustic challenges that need to be addressed to ensure further reductions in noise emissions, as set by the Advisory Council for Aeronautics Research in Europe (ACARE) [1] and the International Civil Aviation Organization (ICAO).

In the framework of the ENOVAL project, Safran Aircraft Engines has designed, manufactured and instrumented test vehicle as well as a 20" UHBR fan stage that is tested in a new facility at Ecole Centrale de Lyon (ECL) in France. This new experimental facility, which is part of the PHARE project supported by the French National Research Agency (ANR), presents ideal conditions for high-quality aeroacoustic measurements of a scaled fan stage that is representative of the state-of-the art turbomachinery. Figure 1 shows the ECL-B3 facility during acoustic tests equipped with a Turbulence Control Screen (TCS) and external microphones mounted on a rotating structure, which is used to measure the upstream fan noise directivity. Wall flush-mounted microphones are used to measure the radiated noise both upstream and downstream of the fan stage. One of the goals of this instrumentation is to decompose the in-duct sound field into acoustic modes, allowing for a better understanding of the noise generation mechanisms. This is the main objective of the current work.

The remainder of the paper is organised as follows. In Section II.A, theoretical aspects of duct acoustics are given along with the array signal processing elements that are required for the modal decomposition approach. In Section III the experimental set-up is briefly described with a focus on how the array was optimized to extend the modal detection capacity. Finally, in Section IV a discussion on the proposed approach and an application on a UHBR fan stage are presented.

*Research Engineer, antonio.pereira@ec-lyon.fr
†Research Engineer at CNRS.
‡Engineer
§Engineer
¶Engineer

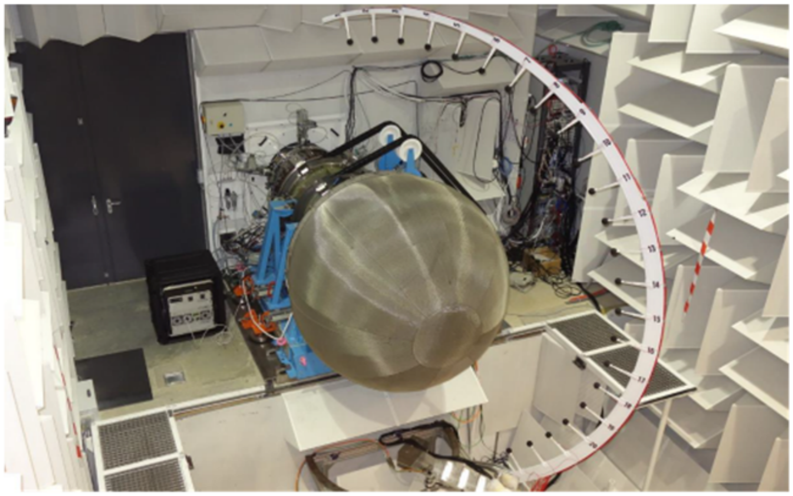

Fig. 1 Turbulence Control Screen (TCS) and external arc of microphones in the anechoic chamber of the ECL-B3 facility.

II. Outline of Theory and Signal Processing Elements

In the first part of this Section, theoretical aspects of duct acoustics are given. The main equations used by the modal decomposition approach are described. The second part presents the technique employed for the modal detection approach.

A. Decomposition of the In-duct Pressure Field into Modes

Modal decomposition or modal identification is a well-known technique used to decompose a complex field (e.g. pressure fluctuations or particle velocity) into an assumed *known* basis. The main assumption is that any complex field may be decomposed into a weighted sum of basis functions (e.g. duct modes, vibrational modes of a plate, acoustic modes in a cavity/room, radiating modes of a complex sound source). The physical understanding of the problem of interest usually gives us the information on how to construct the basis functions. Taking the example of the pressure field inside a waveguide, the solution of the wave equation with a given set of boundary conditions provides us with the basis functions or modal shapes which are appropriate to decompose the acoustic field. The unknowns of the problem are generally the coefficients or modal amplitudes associated to each modal shape.

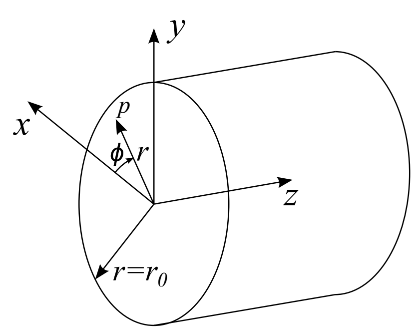

Fig. 2 Sketch of the cylindrical coordinates system.

From now on, the analysis is focused on the pressure field constrained to an enclosure with assumed known boundary conditions. More particularly, the acoustic pressure inside an infinite cylindrical duct with hard walls may be expanded as follows [2]

$$p(z,r,\phi) = \sum_{m=-\infty}^{\infty} \sum_{n=0}^{\infty} \left[A_{m,n} \mathrm{e}^{\jmath k^{+}_{m,n} z} + B_{m,n} \mathrm{e}^{\jmath k^{-}_{m,n} z} \right] f_{m,n}(r) \mathrm{e}^{\jmath m\phi}, \tag{1}$$

where use has been made of the cylindrical coordinates shown in Fig. 2 and $A_{m,n}$ and $B_{m,n}$ are the complex-valued coefficients of modes propagating downstream and upstream, respectively. The subscripts m and n are the azimuthal and radial mode indices, respectively, and $f_{m,n}(r)$ is a normalized modal shape factor (see Ref. [3]) that is written here as

$$f_{m,n}(r) = \frac{J_{|m|}(k_{r,m,n}r)}{\Gamma_{m,n}}, \tag{2}$$

where $k_{r,m,n}$ is to be defined in the following paragraphs and $\Gamma_{m,n}$ is a normalization factor introduced to ensure that the modal shape functions are orthonormal, i.e. orthogonal and normalized over the duct cross-section. In Eq. (1), the $k^{\pm}_{m,n}$ terms are the axial wavenumbers in the downstream ($^+$) and upstream ($^-$) directions and are given by

$$k^{\pm}_{m,n} = -\frac{M_z}{\beta^2}k_0 \pm \hat{k}_{r,m,n}, \tag{3}$$

where $M_z = U_0/c$ is the Mach number along the z-direction, $\beta^2 = 1 - M_z^2$ and $k_0 = \omega/c$ is the acoustic wave number. The $\hat{k}_{r,m,n}$ term is given by:

$$\hat{k}_{r,m,n} = \frac{1}{\beta^2}\sqrt{k_0^2 - \beta^2 k^2_{r,m,n}}, \tag{4}$$

where $k_{r,m,n}$ is a radial wavenumber which is obtained by using the boundary conditions at the duct wall, i.e. at $r = r_0$. Assuming a hard-wall condition, the particle velocity or the derivative of the acoustic pressure with respect to r is zero, and the following condition must be fulfilled:

$$J'_{|m|}(\lambda_{m,n}) = J'_{|m|}(k_{r,m,n}r_0) = 0, \tag{5}$$

where $J'_{|m|}(\cdot)$ corresponds to the first derivative of the mth order Bessel function $J_{|m|}(\cdot)$ and r_0 is the duct internal radius, , as shown in Fig. 2. It should be noted that $\lambda_{m,n}$ is the eigenvalue for a dimensionless radius or $r_0 = 1$. For a given value of azimuthal order $|m|$, the n-th root $\lambda_{m,n}$ of $J'_{|m|}(\lambda_{m,n}) = 0$ gives the radial wavenumber:

$$k_{r,m,n} = \frac{\lambda_{m,n}}{r_0}. \tag{6}$$

It should be noted that for the particular case of zero mean flow velocity ($U_0 = 0\mathrm{m/s}$, $M_z = 0$ and $\beta^2 = 1$) the axial wavenumber $k^{\pm}_{m,n}$ in Eq. (3) reduces to

$$k^{+}_{m,n} = k^{-}_{m,n} = \sqrt{k_0^2 - k^2_{r,m,n}}, \tag{7}$$

which implies that the axial wavenumber of both downstream and upstream propagating waves is the same. Instead of doing a complete modal decomposition for both azimuthal and radial mode coefficients, the simplified case of azimuthal-only decomposition is investigated here. Following these lines, the expansion in Eq. (1) may also be written in the following compact form

$$p(z, r, \phi) = \sum_{m=-\infty}^{\infty} C_m(z, r)\mathrm{e}^{\jmath m\phi}, \tag{8}$$

which gives the acoustic pressure field in terms of azimuthal modes only, the coefficients $C_m(z, r)$ are then given by

$$C_m(z, r) = \sum_{n=0}^{\infty} \left[A_{m,n}\mathrm{e}^{\jmath k^{+}_{m,n}z} + B_{m,n}\mathrm{e}^{\jmath k^{-}_{m,n}z}\right] f_{m,n}(r). \tag{9}$$

It should be noted that the dependency of the azimuthal modal coefficients C_m on z and r is made explicit to emphasize that they are given for a fixed axial section z and radial position r. The coefficients $C_m(z, r)$ in Eq. (8) can be obtained for instance by a Discrete Fourier Transform (DFT) in the azimuthal direction, such as:

$$C_m(z_0, r_0) = \frac{1}{N_\phi}\sum_{l=0}^{N_\phi - 1} p(z_0, r_0, \phi_l)\mathrm{e}^{-\jmath m\phi_l}, \tag{10}$$

where N_ϕ is the number of azimuthal microphone positions, ϕ_l is the angular position of the $l-$th microphone and z_0 and r_0 are respectively any fixed axial and radial positions. The application of the DFT requires the sensors to be equally spaced over the azimuthal direction. In this case, according to the Shannon-Nyquist sampling theorem, the azimuthal sensor spacing should be less than or equal to half the maximum azimuthal wavelength λ_m of interest. In the following, a matrix notation is used and Eq. (8) is conveniently expressed as

$$\mathbf{p} = \mathbf{\Phi}\mathbf{c}, \tag{11}$$

where $\mathbf{p} \in \mathbb{C}^{M\times 1}$ is a vector with measured complex-valued pressure at given frequency ω, $\mathbf{c} \in \mathbb{C}^{N\times 1}$ is a vector containing the complex modal coefficients C_m and $\mathbf{\Phi} \in \mathbb{C}^{M\times N}$ a matrix with complex exponentials constructing the azimuthal modal basis. If the assumption of stationarity and ergodicity of measured time signals holds, one convenient formulation may be used by defining the cross-spectral matrix of measurements as $\mathbf{S_{pp}} \triangleq \mathbb{E}\{\mathbf{pp}^H\}$. Where the operator $\mathbb{E}\{\cdot\}$ is to be understood as the expected value over the number of snapshots, as obtained by segmenting the time signal into short-time blocks then Fourier transforming. Equation (11) then reads

$$\mathbf{S_{pp}} = \mathbf{\Phi}\mathbf{S_{cc}}\mathbf{\Phi}^H, \tag{12}$$

where $\mathbf{S_{cc}}$ is a modal cross-spectral matrix with amplitude of mode coefficients in the diagonal. In the next section it is shown how to estimate the cross-spectral matrix $\mathbf{S_{pp}}$ from sequential measurements.

B. Modal Decomposition Using Sequential Array Measurements

As it will be seen on the experimental setup (see Section III), the fan rig supports microphones mounted on rotating rings. These can be sequentially rotated to scan the wall-pressure field with a fine spatial discretization. The advantage is that the application of modal decomposition approaches may be extended to higher frequencies due to a shift in aliasing. Moreover, a dense spatial discretization may be obtained with a limited number of microphones which allows a cost reduction related to the saving in acquisition channels. The difficulty, however, is that the signal acquisition on sequential positions are not simultaneous which requires the application of advanced signal processing techniques. This is the subject of this section.

With regard to the strategy of sequential measurements it is clear that the phase relationships between moving sensors at successive positions are lost, and therefore the respective cross-spectra cannot be measured. However, the application of modal decomposition methods strongly depends on the phase relationships between the multiple sensor positions. One solution is to use fixed microphones as references, since the cross-spectra between moving and static sensors can be estimated at each step.

An "incomplete" or "*partial*" Cross-Spectral Matrix (CSM) is obtained at the end, the matrix being rectangular whose columns correspond to the moving sensors at successive positions and the rows to the fixed microphones. The next step is then to estimate the cross-spectra between all combinations of moving microphones. Several methods exist to achieve this, among which, two are briefly described in this paper. The first method aims at estimating *holograms* or complex pressure vectors and the second one proposed a method to reconstruct the complete Cross-Spectral Matrix. Both methods are based on the complete cross-spectral matrix between the fixed (or reference) sensors and the *partial* cross-spectral matrix between fixed and moving sensors. The first method is based on Principal Spectral Analysis (PSA) and the second method on matrix products. The details and derivations of the two methods are omitted here, only the main results are presented for brevity.

Noting by $\mathbf{S_{mr}} \in \mathbb{C}^{M\times R}$ the rectangular matrix ($M > R$) storing the cross-spectra between the M successive sensor positions and R fixed references and $\mathbf{S_{rr}} \in \mathbb{C}^{R\times R}$ the complete cross-spectral matrix of fixed sensors (references), one can write [4–6]

$$\mathbf{X} = \overline{\mathbf{S}}_{\mathbf{mr}}\overline{\mathbf{\Psi}}\lceil\sqrt{\Sigma}\rfloor^{-1}, \tag{13}$$

where the notation $\overline{\mathbf{A}}$ stands for the conjugate of matrix $\mathbf{A}$ and the matrices $\mathbf{\Psi}$ ans Σ result from an eigenvalue decomposition of the cross-spectral matrix of references, such as:

$$\mathbf{S_{rr}} = \mathbf{\Psi}\lceil\Sigma\rfloor\mathbf{\Psi}^H, \tag{14}$$

where the notation $\mathbf{A}^H$ stands for the conjugate-transpose (Hermitian) of the matrix $\mathbf{A}$, $\mathbf{\Psi} \in \mathbb{C}^{R\times R}$ is a matrix containing eigenvectors and $\Sigma \in \mathbb{R}^{R\times R}$ a diagonal matrix with eigenvalues on the diagonal elements. This decomposition is often referred to as decomposition decomposition into *virtual sources*. Indeed, by definition, Eq. (14) decomposes the $\mathbf{S_{rr}}$ matrix into independent (or uncorrelated) components since Σ is a diagonal matrix. The denomination *virtual sources* results from the fact that this is a purely mathematical decomposition. Thus, only at very particular cases the different components carry a physical meaning and do correspond to *real sources*. In addition, the decomposition in Eq. 14 is performed independently at each frequency, and the values and eigenvectors are ordered in descending order. Therefore nothing prevents a given virtual source from switching between different combinations of eigenvalues and eigenvectors depending on the frequency.

The result from Eq. (13), i.e. $\mathbf{X} \in \mathbb{C}^{M\times R}$, is a matrix in which each column $[\mathbf{x}_1\ \mathbf{x}_2\ \cdots\ \mathbf{x}_R]$ corresponds to the contribution of a *virtual source*. Then, modal decomposition methods are applied to each component of $\mathbf{X}$ independently. The final result is obtained by the sum in amplitude of the contribution due to all the considered virtual sources.

The goal of the second method used in this study is to reconstruct the complete cross-spectral matrix between all sensor positions. This is achieved by using the following formulation [4, 7]:

$$\mathbf{S_{mm}} = \mathbf{S_{mr}}\mathbf{S_{rr}^{\dagger}}\mathbf{S_{mr}^{H}}, \tag{15}$$

where the symbol$\cdot^{\dagger}$ represents the pseudo-inverse of a matrix and $\mathbf{S_{mr}}$ being the cross-spectral matrix called *partial*, as defined before Eq. (13). It is important to note that by these two methods, only the part of the cross-spectral matrix $\mathbf{S_{mm}}$ that is consistent with the set of selected fixed references can be reconstructed. If the number of fixed references is small as compared to the number of actual independent sources, some sources cannot be reconstructed. In other words, the results of the modal decomposition will reflect the contribution of the largest R sources, where R is the number of fixed references. It should also be noted that these two methods are equivalent if all the virtual sources in $\mathbf{X}$ are considered. In this sense, the so-called PSA method has an advantage when few physical sources are present. This is because only the high energy components related to actual sources need to be considered, the weaker components being neglected. Neglecting the weaker components can improve the Signal-to-Noise Ratio (SNR) since they are often associated with measurement noise.

Finally, modal decomposition methods are applied either from the complete cross-spectral matrix $\mathbf{S_{mm}}$ or from the "holograms" in $\mathbf{X}$, which are linked to the virtual sources. For the latter, the modal decomposition is applied independently at each column of $\mathbf{X}$, also known as principal component. This is written as

$$\mathbf{x}_i = \mathbf{\Phi}\mathbf{c}_i, \tag{16}$$

for the i-th principal component and thus $[\mathbf{x}_1 = \mathbf{\Phi}\mathbf{c}_1, \mathbf{x}_2 = \mathbf{\Phi}\mathbf{c}_2, \cdots, \mathbf{x}_R = \mathbf{\Phi}\mathbf{c}_R]$ for R components. Note that $\mathbf{c}_i$ are complex mode amplitudes corresponding to the i-th principal component and $\mathbf{x}_i$ is replacing $\mathbf{p}$ at the Eq. (11). The result for each component is independently obtained from

$$\hat{\mathbf{c}}_i = \mathbf{\Phi}^{\dagger}\mathbf{x}_i, \tag{17}$$

and therefore the contribution due to all components given by $\hat{\mathbf{c}} = \sum_{i=1}^{R} |\hat{\mathbf{c}}_i|^2$. The notation $\hat{\mathbf{a}}$ stands for an estimate of $\mathbf{a}$. For the second case, the direct problem is written by

$$\mathbf{S_{mm}} = \mathbf{\Phi}\mathbf{S_{cc}}\mathbf{\Phi}^{H}, \tag{18}$$

with $\mathbf{S_{cc}}$ the modal cross-spectral matrix whose mode amplitudes are on the diagonal and $\mathbf{S_{mm}}$ representing $\mathbf{S_{pp}}$ from Eq. (12). The solution of this type of problem can be estimated from

$$\hat{\mathbf{S}}_{\mathbf{cc}} = \mathbf{\Phi}^{\dagger}\mathbf{S_{mm}}(\mathbf{\Phi}^{\dagger})^{H}. \tag{19}$$

The solution of the modal decomposition problem, see Eqs. (17) and (19), are generically written in terms of the pseudo-inverse of the modal matrix $\mathbf{\Phi}$ for simplicity. Several advanced methods have been proposed to solve this inverse problem [8–18]. The choice of a specific method will depend on the nature and properties of the studied noise source. For instance, different methods will be more adapted to either broadband or tonal noise. Tonal noise is characterized by constructive interference phenomena which tend to favor a small set of particular modes. Thus, methods that enforce sparse solutions are more suitable in this case. This is less the case for broadband noise since a large number of modes with similar amplitude contribute to the total acoustic power. In this work, classic beamforming and an inverse method with adjustable sparsity degree [19] are applied to the measured data.

III. Experimental Setup of a 20” UHBR Fan Stage

The UHBR fan stage, which presents a diameter of D_{Fan} = 20 in (0.508 m), has been highly instrumented for acoustic measurements. Upstream noise directivity can be measured using a 27-microphone array that nearly covers a 2 m semi-sphere. Additionally, the UHBR fan stage can be equipped with up to 160 in-duct wall-pressure microphones. In this paper, 123 microphones will be used for modal detection analysis of upstream, interstage and downstream noise from the fan/OGV stage.

A. Azimuthal rotating microphone arrays

1. Upstream measurements

The upstream instrumentation includes 31 wall-pressure microphones. Experimental measurements have been performed with 1/4 in GRAS 46BG microphones that have been flushed-mounted without their protection grid.

A schematic of the microphone set-up is shown in Figure 3. Fixed microphones are placed at two axial positions. These can be used as a reference (see Section II.B) to synchronize the sequential measurements of the microphones on the upstream rotating ring. Such a rotating ring is composed of 16 microphones located at the same axial station, close to the fan blades leading edges, with a uniform azimuthal spacing of $2\pi/18$ except for 2 microphones that are spaced of $2\pi/9$ for integration constraints.

In the absence of ring rotations and based on the azimuthal distribution of microphones, it is possible to estimate the maximum azimuthal order m at which the modal decomposition can be calculated without aliasing. For a configuration of equally spaced microphones, m is given by the Shannon-Nyquist sampling theorem, which states that at least two samples per wavelength are necessary. This can also be evaluated by computing the mutual coherence between a pair of modes for a given microphone distribution [17, 20]. This parameter indicates how similar two different modes are “seen” by the microphone array. If the mutual coherence is equal to 1 for a pair of modes, it means that the two modes are seen identically by the array and thus they cannot be separated.

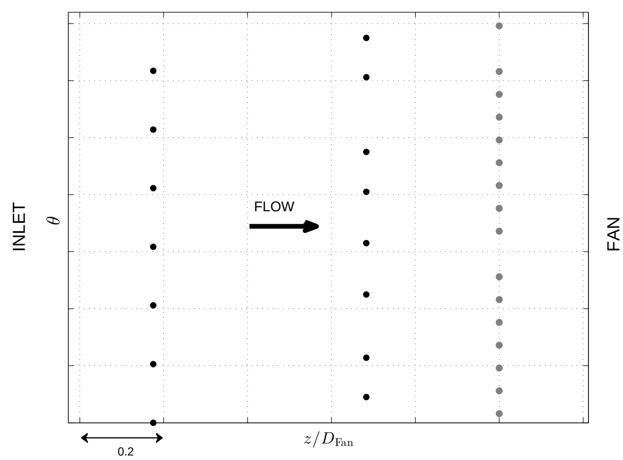

Fig. 3 Schematic representation of GRAS 46BG microphone positions for upstream modal detection, where z/D_{Fan} corresponds to a non-dimensional axial distance. Fixed microphones are represented by black circles. Microphones installed on a rotating ring are shown in gray circles.

The mutual coherence computed based on the 16 microphones array from Figure 3 is shown in Figure 4. It can be seen that modes are properly separated up to an azimuthal order of m=9, above this threshold the maximum mutual coherence is equal to one. This implies that there is at least two modes that cannot be distinguished. Considering the duct diameter of the machine, this corresponds to a frequency of about 2.3 kHz. If one wishes to perform a modal decomposition at higher frequencies, the ring array must be rotated in order to increase the number of spatial samples. A question that arises is how to wisely rotate the rings in order to minimize the number of rotations while increasing the frequency range of analysis. To answer the above question an optimization process has been employed to find the best configuration of ring rotations. The idea is to perform a fixed number of random rotations to the initial equally spaced array and evaluate the mutual coherence parameter. A Monte Carlo approach with about 1000 random trials is used in order to reach an optimal configuration. An example of this optimization process is shown at the Fig. 5. For the

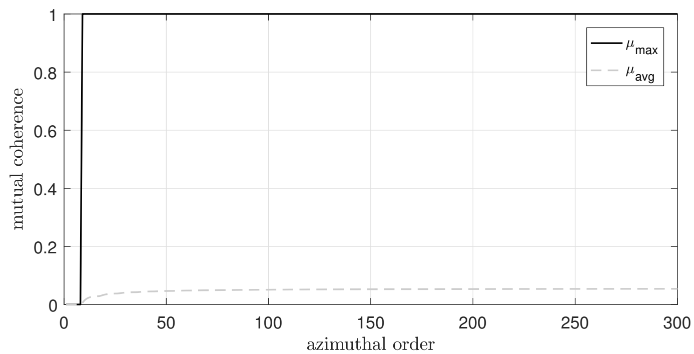

Fig. 4 Mutual coherence obtained from an azimuthal array with 18 equally spaced microphones.

present test campaign a configuration using 14 rotations has been chosen, leading to a number of 15 ring positions. This represents a good compromise between the number of ring rotations and the highest azimuthal order that can be reached.

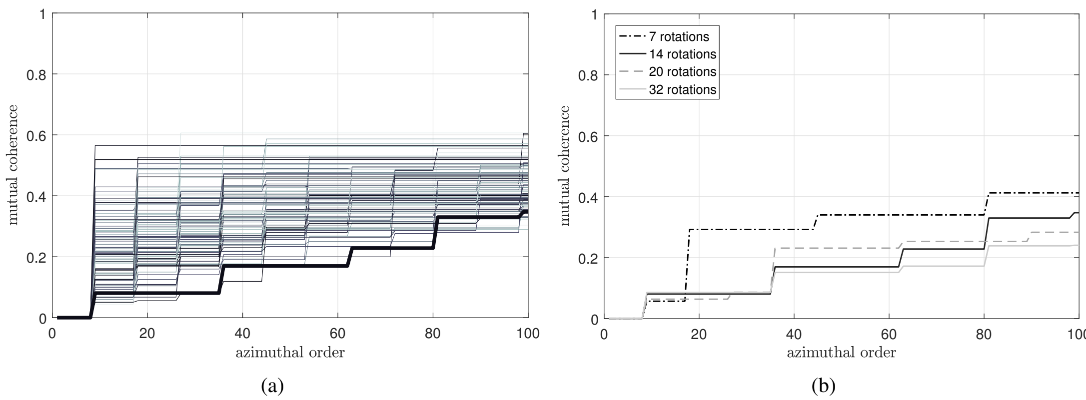

Fig. 5 Example of the optimization process to select an optimal number of ring rotations and rotation steps. (a) Mutual coherence of several trials evaluated for a set of 14 random rotation steps. The configuration leading to the lowest mutual coherence is highlighted in black. (b) Lowest mutual coherence level for different numbers of rotations.

2. Inter-stage measurements

Interstage instrumentation is defined by 11 wall-pressure microphones placed at three different axial positions as shown in Figure 6. Downstream of the fan stage, 6 microphones 1/4 in GRAS 46BG are uniformly distributed on the rotating ring at the axial section close to the fan blades trailing edge. According to the Shannon-Nyquist sampling theorem, the rotating ring can identify azimuthal modes up to m=3 in the absence of rotations. To overcome this limitation, it is necessary to increase the number of azimuthal measurement positions with the ring rotations. To synchronize sequential measurements, fixed Kulite MIC-062 and GRAS 47BX-S6 microphones have been installed in the interstage, as shown in Figure 6. As the upstream part, microphone grids protective has been dismantled to have a membrane flush mounting integration.

3. Downstream rotating rings

The downstream instrumentation consists of up to 81 wall-pressure microphones. A schematic of the microphone distribution is shown in Figure 7. In-duct microphone arrays are installed over an axial length of about $1.2D_{Fan}$, where D_{Fan} is the fan diameter. It is possible to distinguish four different groups of microphone arrays. The first group is placed behind the OGV and is composed of 10 fixed GRAS 47BX-S6 microphones. The second group includes 2 GRAS 46BG microphones installed at the same axial position on a rotating ring. Downstream ring rotations are independent of

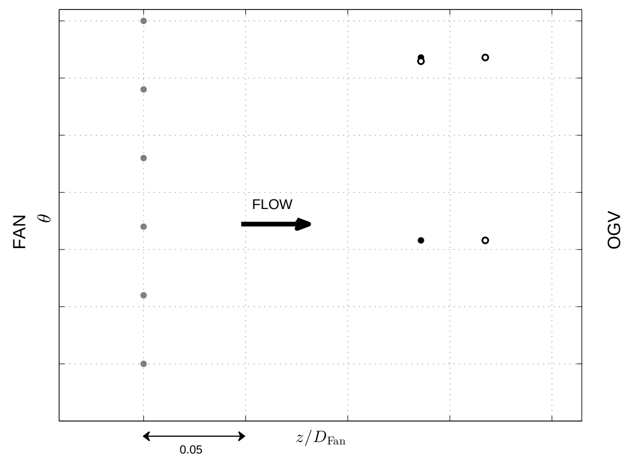

Fig. 6 Schematic representation of microphone positions for interstage modal detection. Microphones GRAS 46BG installed on rotating ring are represented by gray circles. Fixed sensors, GRAS 47BX-S6 and Kulite MIC-062 pressure transducers are represented by filled and empty black circles, respectively.

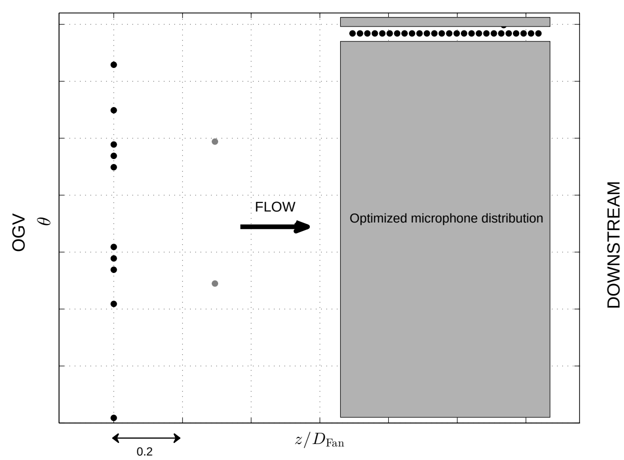

Fig. 7 Schematic representation of the microphone positions for downstream modal detection. Fixed microphones are represented by black circles. Microphones installed on rotating rings are represented by gray circles.

those from upstream and interstage rotating rings. The third group is placed further downstream and is composed of 30 fixed GRAS 46BG microphones where the location have been optimized over an axial length of $0.6D_{Fan}$. Finally, an axial line array composed of 26 GRAS 46BG microphones is located in the same region. This last instrumentation is mainly dedicated to the analysis of axial wavenumbers. Nevertheless all fixed downstream microphones can be exploited to synchronize rotating microphones for the azimuthal modes detection.

This experimental setup can be used for different types of modal analysis. Using the 2 microphones located at the same axial position on the rotating ring, it is possible to perform an azimuthal duct mode decomposition of the downstream noise spectra. In this case, all fixed microphones can be used as a reference to synchronize sequential measurements from the ring rotation. Using all microphones on the rotating ring a complete modal analysis can be performed to identify azimuthal and radial modes. It should be noted that the rotation of the microphone rings is necessary to increase the high frequency resolution of the modal analysis. A similar procedure as the one presented in Section III.A.1 have been used to optimize the rotating angles.

IV. Results & Discussion

A. Azimuthal modal decomposition using rotating arrays

1. Influence of the number of rotations

In order to evaluate the impact of the number of array rotations, azimuthal decomposition maps are computed with the initial array and increasing number of rotations. This is done using the 16-microphones ring array at the inlet (see section III.A.1). Classical beamforming is used as the method for this comparison since in this case results do not depend on the azimuthal extent of the mode maps. Remember that beamforming scans the range of azimuthal orders treating each order independently. The same azimuthal extent is kept for all studies cases. Results are shown for 2, 5, 10 and 15 rotations. It can be seen for the no rotation case (see Figure 8(a)) that results are largely disturbed by aliases. Notice that replicated patterns are shifted by multiples of 18 and at an azimuthal order of $m = 9$ they overlap the central part of the diagram. This shows the upper frequency limit of alias-free results for the case of no ring rotation. As predicted by the theory in Section III.A.1 it corresponds to a frequency of about 2 kHz. This value is prone to change at different rotational speeds due to the increase on the number of cut-on modes as the mean flow velocity increases. Looking at results with increasing number of ring rotations, see Figures 8(a), (b) and (c), it can be seen that the replicas are progressively reduced. The final result with 15 ring positions allows a considerable increase on the upper frequency limit.

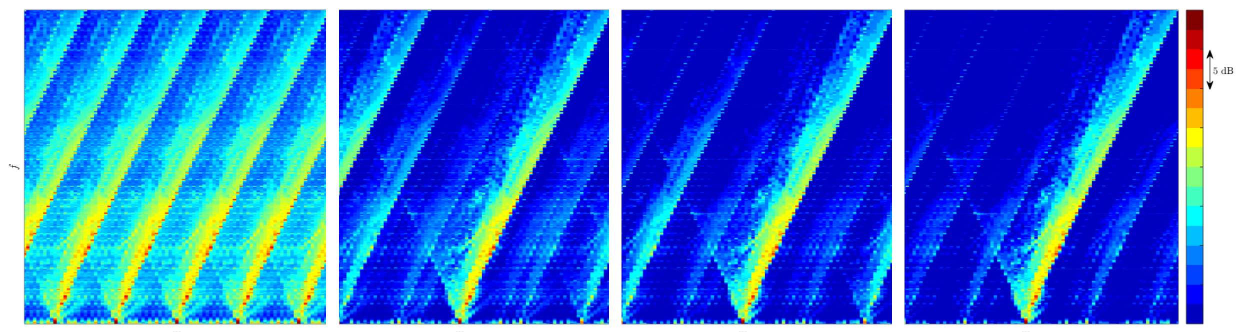

(a) 1 ring position (b) 5 ring positions (c) 10 ring positions (d) 15 ring positions

Fig. 8 Amplitude of azimuthal m mode coefficients versus frequency. Results are shown for increasing number of ring rotations, namely: (a) 1 ring position, (b) 5 ring positions, (c) 10 ring positions and (d) 15 ring positions. The modal amplitudes are estimated using classical beamforming at an operating point representative of approach, that is, 50% of the nominal drive.

2. Comparison of post-processing methods

The estimation of the modal amplitudes, that is, how to solve equation (18) may be done by different methods and assumptions. Here a comparison is made between classical beamforming and an iterative Bayesian Inverse Approach (iBIA) [19, 21]. Beamforming being a reference of a fast and robust method it justifies this choice here. However, its limitations are two-fold, first is the assumption that modal coefficients are mutually incoherent, and second the fact that the array response remains in the solution which limits the resolution. With the aim to overcome these limitations, an iterative inverse method is applied. The array located downstream of the fan/OGV stage is used for the comparison. As explained in Section 7, 2 microphones located at the same axial position are sequentially rotated 15 times such as to obtain 30 azimuthally independent positions. Results for beamforming and iBIA are shown in Figure 9. Two main features are worth noting from the comparison of methods. First, replicated amplitudes due to aliasing are largely attenuated by the iBIA method as compared to beamforming. Second, the dynamic range of results is well improved, switching from about 10dB with beamforming to 25dB with iBIA. The latter is used as a reference for all the following results.

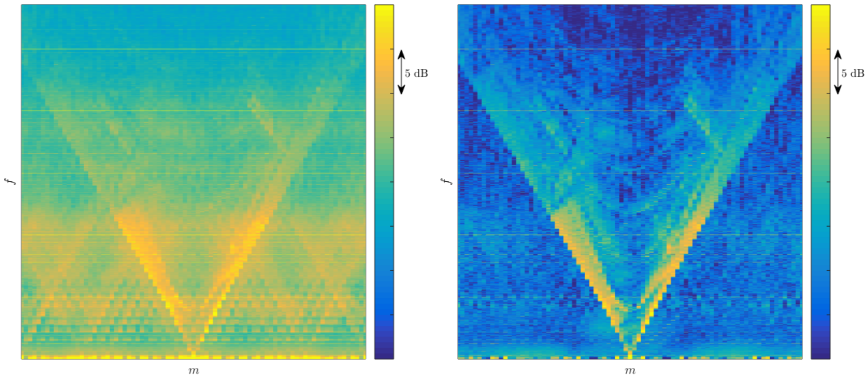

(a) (b)

Fig. 9 Amplitude of azimuthal mode coefficients as a function of frequency resulting from two different methods, namely: (a) beamforming and (b) iterative Bayesian Inverse Approach (iBIA). Results are obtained at a section downstream of the fan/OGV stage, see Figure 7, at approach conditions.

3. Impact of the acquisition time

The use of wall-flush mounted microphones under a flow results in a low signal-to-noise ratio, specially if the probes are spaced several wavelengths apart. Thus long acquisition times are required. A duration of 300 seconds has been chosen based on the analysis of a companion paper [22]. In addition, the "synchronization" approach used here heavily depends on the cross-spectra between moving and fixed microphones. Since their separation distance is relatively large (see Figure 3) the rate of convergence of cross-spectral coefficients is slow. In order to show the impact of acquisition time on the modal coefficients, results are computed using different signal lengths. Results are shown in Figure 10 for signal lengths equal to 30s, 60s, 120s and 300s. It can be seen from results with 30s acquisition time that the modal amplitude maps are impaired by aliased components, see Figure 10(a). This could lead to a misinterpretation of results as aliased components overlap the useful part on V-shaped mode diagrams. As longer acquisition times are used, the energy of aliased components are slowly reduced, see Figures 10(b)-(d). The acquisition time of 300s used in the experimental campaign allows a well-enough reduction of aliasing over the frequency band of interest. All the following results are thus computed with 300s acquisition time, 15 ring positions and the iBIA method.

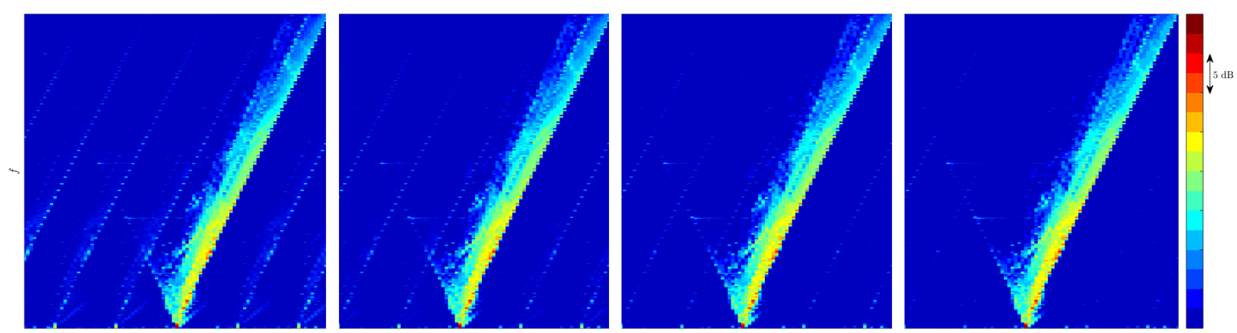

(a) T_s = 30s (b) T_s = 60s (c) T_s = 120s (d) T_s = 300s

Fig. 10 Amplitude of azimuthal m mode coefficients versus frequency. Impact of the acquisition time over the estimated modal amplitudes. Results are shown for increasing length of acquisition time T_s, namely: (a) 30s, (b) 60s, (c) 120s and (d) 120s. An operating point representative of approach conditions is kept for the study.

4. Upstream azimuthal modal content

In this section the broadband modal content estimated upstream of the rotor is evaluated. The results are shown for three operating conditions representative of approach, cutback and sideline, see Figure 11. It can be seen that the modal content is predominantly co-rotating, positive azimuthal order m represent modes spinning at the same direction as the fan. To be noticed also is that most of the energy is located towards the boundary between cutof/cuton boundary. Comparing the amplitudes from approach, cutback and sideline, it is interesting to note that levels are higher at cutback (80%ND). One hypothesis for this is that at higher speeds, the formation of shock waves at the blade tips blocks the noise generated downstream of the rotor blades to propagate upstream.

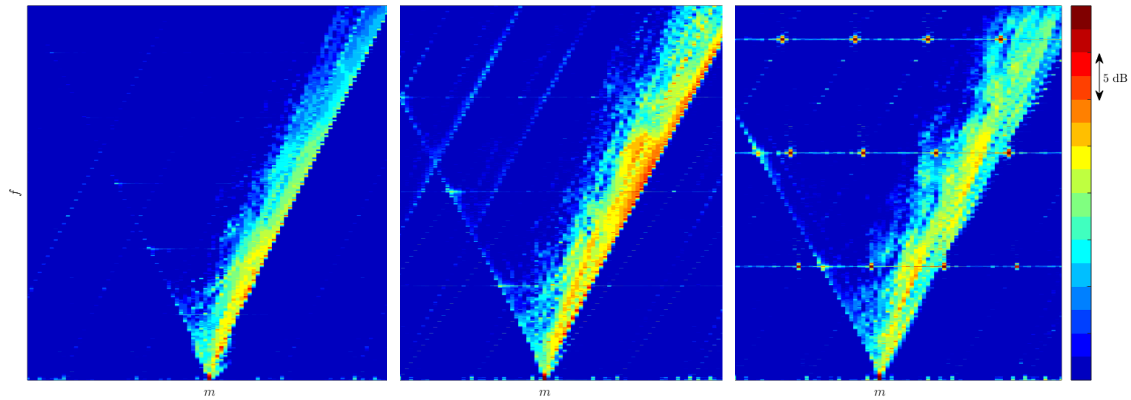

(a) approach (b) cutback (c) sideline

Fig. 11 Inlet azimuthal mode spectra. Results are shown for three operating points representative of (a) approach 55%**ND, (b) cutback** 80%**ND and (c) sideline** 95%**ND. Modal coefficients are estimated using iBIA method with 300s acquisition time.**

5. Inter-stage azimuthal modal content

Broadband azimuthal mode plots at the interstage are shown in Figure 12. This data is estimated using the 6-microphones array which is rotated 15 times leading to 90 azimuthal positions. As before, results are computed at approach, cutback and sideline conditions. It can be noticed the rotation of V-shape diagrams due to swirl in the inter-stage. Again, higher levels are observed for co-rotating modes, although with more energy at the counter-rotating part as compared to the inlet. To be noticed also is the appearance of high amplitudes at lower frequencies in the cutoff region. One explanation is the impingement of rotor wakes at the microphones that creates a large hydrodynamic component. Notice that the slope of the spot is changed with an increase on the fan rotational speed.

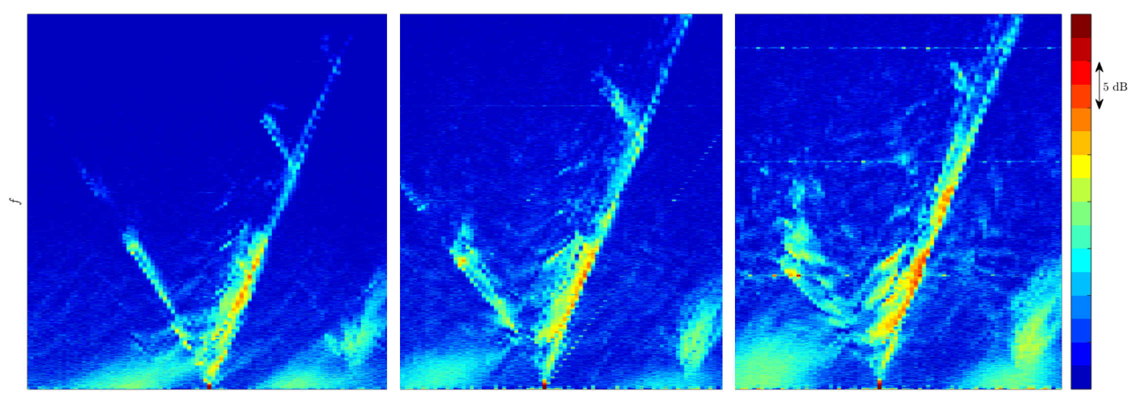

(a) approach (b) cutback (c) sideline

Fig. 12 Inter-stage azimuthal mode spectra. Results are shown for three operating points representative of (a) approach 55%**ND, (b) cutback** 80%**ND and (c) sideline** 95%**ND. Modal coefficients are estimated using iBIA method with 300s acquisition time.**

6. Downstream azimuthal modal content

Azimuthal mode spectra estimated at the by-pass duct downstream of the fan/OGV stage is shown in Figure 13. The results have been computed using a 2-microphones array which is rotated 15 times leading to 30 independent azimuthal positions. A total number of 56 fixed microphones have been used as references for the synchronization approach. Contrary to the inlet and inter-stage mode spectra, a more even balance between co- and counter-rotating modes is observed in the downstream section. However, it can be noticed that at higher speeds, namely 80% and 95%ND, more energy is seen on counter-rotating modes in a frequency band ranging from 3kHz up to 7 kHz. This is true for modes with higher cut-on ratios, which appear in the mode spectra in the interior of V-shape diagrams.

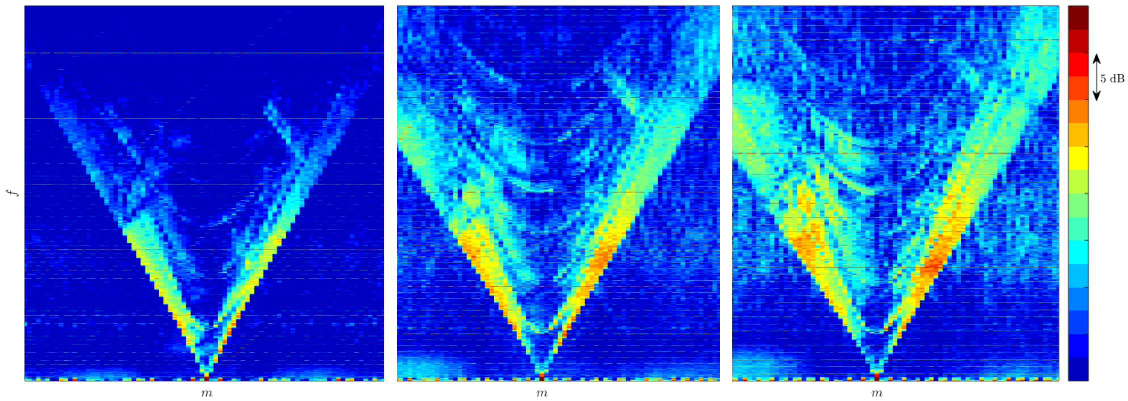

(a) approach (b) cutback (c) sideline

Fig. 13 Downstream azimuthal mode spectra at the by-pass section. Results are shown for three operating points representative of (a) approach 55%ND, (b) cutback 80%ND and (c) sideline 95%ND. Modal coefficients are estimated using iBIA method with 300s acquisition time.

7. Modal content at tonal components

A technique using a synchronous average has been applied to single-out the tonal component of the noise radiated by the fan/OGV stage. The idea is to use the signal recorded by a laser tachometer to resample the signal not in time but in angle. The resampled signal can be averaged over one or more shaft cycles. Thus, the portion of signal coherent to the rotational speed is constructively averaged while the random part is destructively averaged. At the end, only the deterministic part of the signal is kept. In other words, the resampling step allows for the transformation of the measured wall-pressure signals from time to angle, i.e.: $p(t) \to p(\theta)$. Then, the signal averaged over one or more cycles is described here by [23]

$$\hat{p}_m[\theta] = \frac{1}{K}\sum_{k=0}^{K-1} p[\bar{\theta} + k\Theta], \tag{20}$$

where $\bar{\theta}$ is a block of signal containing one or more complete revolutions and Θ the duration or size of each block. Finally, a residual signal can be obtained by subtracting the averaged signal from the raw signal, as follows:

$$\hat{p}_r(\theta) = p(\theta) - \hat{p}_m(\theta), \tag{21}$$

and therefore the deterministic part is removed from the raw signal. In other words, this procedure allows for the extraction of 1st order cyclostationary components from the measured signal, the residual part $\hat{p}_r$ containing 2nd and higher orders of cyclostationarity [23]. An example of spectra obtained after this procedure is shown in Fig. 14 for microphones at the inlet, inter-stage and at the by-pass section. Looking at the residual spectra computed from $\hat{p}_r(\theta)$, it can be seen that the tones are largely reduced. Reductions of more than 20 dB are observed. At the inlet part of the tonal noise still remains in the residual spectrum at low engine orders and blade passing frequencies, see Figure 14(a). This could be due to some residual upcoming distortion or fan imbalance. Further investigation should be done to better explain this behavior.

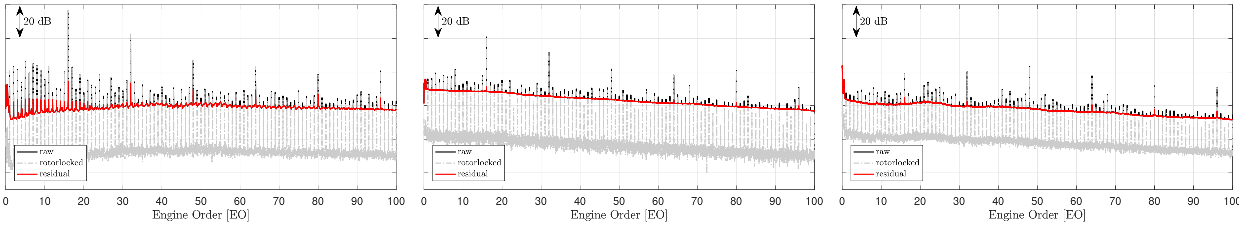

(a) inlet (b) inter-stage (c) by-pass downstream

Fig. 14 Example of spectra after synchronous averaging procedure showing the raw, rotor-locked and residual spectra. Results are shown for microphones at the: (a) inlet, (b) inter-stage and (c) by-pass section.

Finally, the estimation of azimuthal mode amplitudes is done using the data from this analysis. Figure 15 shows the results at the 1st Blade Passing Frequency (BPF) at cutback condition for the upstream, interstage and downstream locations respectively. At this frequency, the modal content is mainly composed of the deterministic part of the signal based on shaft cycles averages, witch corresponds to tonal noise. Except for downstream decomposition, it can be observed that the amplitude of some azimuthal modes is 20 dB above the average. Some azimuthal orders, can be explained by uniform rotor-stator interaction that corresponds to the Tyler and Sofrin's law [24] $m = nB \pm kV$, where B and V are the number of blades and vanes of fan stage respectively, and n and k are integer numbers with $n = 1$ for the example at the 1st BPF. Nevertheless, considering the fan diameter and the Mach number, these modes should be cut-off at this frequency. One possible explanation is that the proximity of the upstream and interstage microphones arrays to the fan blades does not allow the cut-off modes amplitudes to decay.

V. Conclusions and Future Work

Further noise reduction from the next generation of turbofan engines requires an improved understanding of fan noise. To this end, modal decomposition in state-of-the art fan rigs with a large number of in-duct microphones will provide further information about the noise generation and propagation. This will be suitable to improve the design of fan blades, OGVs and acoustic liners. In this context, the feasibility of in-duct modal decomposition in the new ECL-B3 fan test bench has been presented in this paper. In particular, rotatable microphone arrays are used to estimate the modal content at the intake, interstage and downstream of a scaled UHBR fan/OGV stage manufactured by Safran Aircracft Engines. It was shown that the optimization of the array rotating steps and the use of an advanced inverse technique allows for the estimation of the modal content over a wide frequency range. Work is currently ongoing to perform a complete modal break-down at the by-pass section giving further information of the radial modal content.

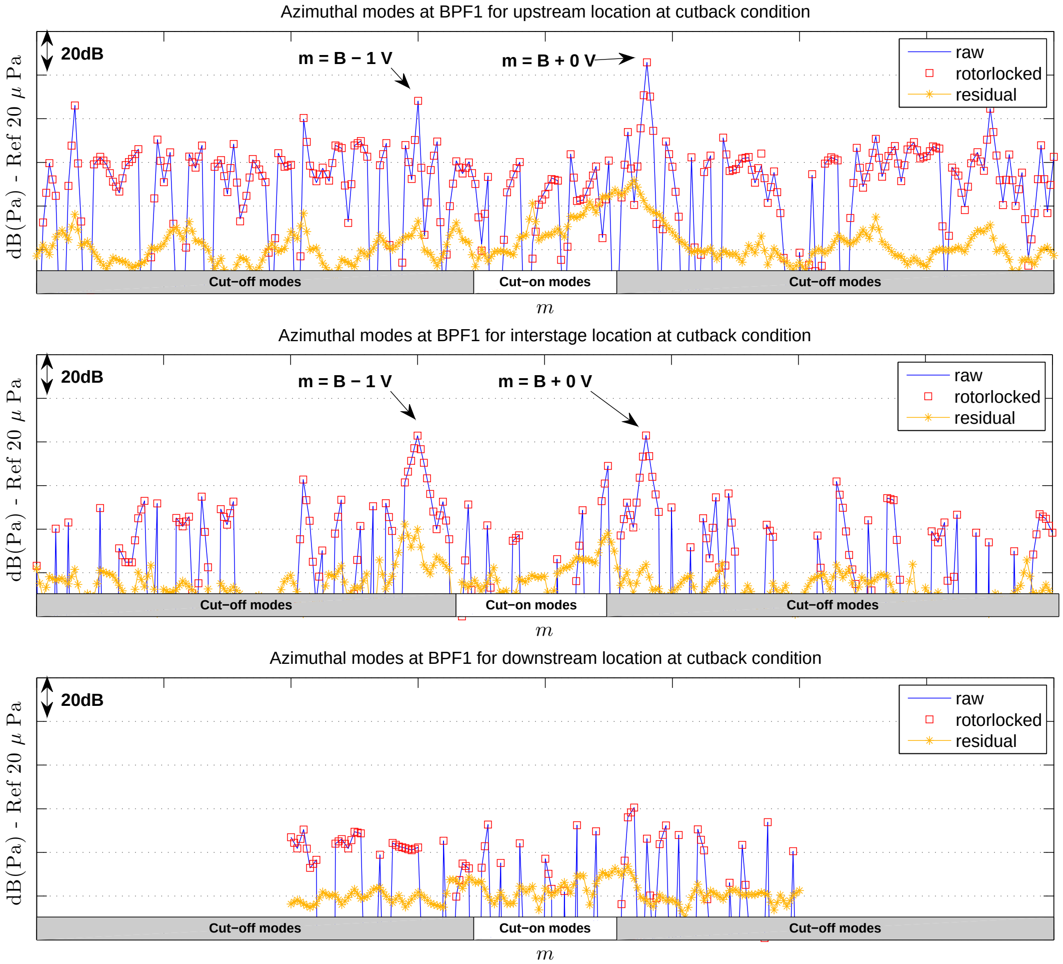

Fig. 15 Modal amplitudes at cutback condition from iBIA method at upstream, interstage and downstream locations for 1st Blade Passing Frequency(BPF). m **correspond to the azimuthal order of modes. Azimuthal detection using raw signal, is noted with blue line. Decomposition between deterministic part of signal (named rotorlocked) and residual part are marked with red squares and orange stars respectively. Cut-on modes area are symbolized by the blank and cut-off modes area are in gray.**

Acknowledgements

The research funding for this project was partially provided by the European Commission (Grant Agreement FP7-604999), as part of the ENOVAL (ENgine mOdule VALidators) project, and Safran Aircraft Engines. This work was performed within the framework of the Labex CeLyA of the Université de Lyon, within the programme "Investissements d'Avenir" (ANR-10-LABX-0060/ANR-16-IDEX-0005) operated by the French National Research Agency (ANR), and is also partially supported by the industrial Chair ADOPSYS co-financed by Safran Aircraft Engines and the ANR (ANR-13-CHIN-0001-01). The authors kindly acknowledge our colleagues from MicrodB for designing and optimising the in-duct microphone arrays.

References

[1] "European Commission, Report of the High Level Group on Aviation, Flightpath 2050 Europe's Vision for Aviation." Tech. rep., 2011.

[2] Munjal, M., *Acoustics of ducts and mufflers with application to exhaust and ventilation system design*, Wiley-Interscience publication, Wiley, 1987.

[3] Tapken, U., and Enghardt, L., "Optimization of sensor arrays for radial mode analysis in flow ducts," *Proceedings of the 12th AIAA/CEAS Aeroacoustics Conference, Cambridge, Massachusetts, USA*, 2006.

[4] Otte, D., "Development and evaluation of singular value analysis methodologies for studying multivariate noise and vibrations problems," Ph.D. thesis, Katholieke Universiteit Leuven, 1994.

[5] Leclère, Q., "Multi-channel spectral analysis of multi-pass acquisition measurements," *Mechanical Systems and Signal Processing*, Vol. 23, No. 5, 2009, pp. 1415 – 1422.

[6] Pereira, A., "Acoustic imaging in enclosed spaces," Ph.D. thesis, INSA de Lyon, 2013.

[7] Yoon, S. H., and Nelson, P. A., "A method for the efficient construction of acoustic pressure cross-spectral matrices," Project Report no 281, University of Southampton, October 1998.

[8] Farassat, F., Nark, D. M., and Thomas, R. H., "The detection of radiated modes from ducted fan engines," *7th AIAA/CEAS Aeroacoustics Conference, Maastricht, The Netherlands, 2001*, 2001.

[9] Lewy, S., "Inverse method predicting spinning modes radiated by a ducted fan from free-field measurements," *The Journal of the Acoustical Society of America*, Vol. 117, No. 2, 2005, pp. 744–750.

[10] Sijtsma, P., "Feasibility of in-duct beamforming," *13th AIAA/CEAS Aeroacoustics Conference, Rome, Italy*, Vol. 3696, 2007, p. 2007.

[11] Castres, F. O., and Joseph, P. F., "Experimental investigation of an inversion technique for the determination of broadband duct mode amplitudes by the use of near-field sensor arrays," *The Journal of the Acoustical Society of America*, Vol. 122, No. 2, 2007, pp. 848–859.

[12] Castres, F. O., and Joseph, P. F., "Mode detection in turbofan inlets from near field sensor arrays," *The Journal of the Acoustical Society of America*, Vol. 121, No. 2, 2007, pp. 796–807.

[13] Bennett, G. J., O'Reilly, C., Tapken, U., and Fitzpatrick, J., "Noise source location in turbomachinery using coherence based modal decomposition," *Proceedings of the 15th AIAA/CEAS Aeroacoustics Conference, Miami, FL, USA*, 2009.

[14] Tapken, U., Raitor, T., and Enghardt, L., "Tonal noise radiation from an UHBR Fan - Optimized in-duct radial mode analysis," *Proceedings of the 15th AIAA/CEAS Aeroacoustics Conference, Miami, FL, USA*, 2009.

[15] Finez, A., Pereira, A., and Leclère, Q., "Broadband mode decomposition of ducted fan noise using cross-spectral matrix denoising," *Proceedings of Fan Noise 2015, Lyon, France*, 2015.

[16] Pereira, A., Finez, A., Leclère, Q., Salze, E., and Souchotte, P., "Modal identification of a small-scale ducted fan," *Proceedings of the 22nd AIAA/CEAS Aeroacoustics Conference, Lyon, France*, 2016.

[17] Behn, M., Kisler, R., and Tapken, U., "Efficient azimuthal mode analysis using compressed sensing," *Proceedings of the 22nd AIAA/CEAS Aeroacoustics Conference, Lyon, France*, 2016.

[18] Pestana, M., Pereira, A., Salze, E., Thisse, J., Sanjosé, M., Jondeau, E., Souchotte, P., Roger, M., Moreau, S., Regnard, J., and Gruber, M., "Aeroacoustics of an axial ducted low Mach-number stage: numerical and experimental investigation," *Proceedings of the 23rd AIAA/CEAS Aeroacoustics Conference*, 2017.

[19] Leclère, Q., Pereira, A., Bailly, C., Antoni, J., and Picard, C., "A unified formalism for acoustic imaging based on microphone array measurements," *International Journal of Aeroacoustics*, Vol. 16, No. 4-5, 2017, pp. 431–456.

[20] Candès, E., and Romberg, J., "Sparsity and incoherence in compressive sampling," *Inverse Problems*, Vol. 23, No. 3, 2007, pp. 969–985. doi:10.1088/0266-5611/23/3/008.

[21] Merino-Martínez, R., Sijtsma, P., Snellen, M., Ahlefeldt, T., Antoni, J., Bahr, C. J., Blacodon, D., Ernst, D., Finez, A., Funke, S., Geyer, T. F., Haxter, S., Herold, G., Huang, X., Humphreys, W. M., Leclère, Q., Malgoezar, A., Michel, U., Padois, T., Pereira, A., Picard, C., Sarradj, E., Siller, H., Simons, D. G., and Spehr, C., "A review of acoustic imaging methods using phased microphone arrays," *CEAS Aeronautical Journal*, 2019. doi:10.1007/s13272-019-00383-4.

[22] Salze, E., Gea-Aguilera, F., Pereira, A., Souchotte, P., Regnard, J., and Gruber, M., "New modular fan rig for advanced aeroacoustic tests - Acoustic characterization of the facility," *Proceedings of the 25th AIAA/CEAS Aeroacoustics Conference, Delft, Netherlands*, 2019.

[23] Antoni, J., "Cyclostationarity by examples," *Mechanical Systems and Signal Processing*, Vol. 23, No. 4, 2009, pp. 987 – 1036.

[24] Tyler, M., and Sofrin, T. G., "Axial Flow Compressor Noise Studies," *Society of Automotive Engineers Transactions*, Vol. 70, 1962, pp. 309–332.